

Shape Analysis of Giant Vesicles With Fluid Phase Coexistence by Laser Scanning Microscopy to Determine Curvature, Bending Elasticity, and Line Tension

Samuel T. Hess, Manasa V. Gudheti, Michael Mlodzianoski, and Tobias Baumgart

Summary

Membrane shape parameters such as curvature, bending elasticity, and lateral tension, are relevant to the lateral organization and function of biomembranes, and may critically influence the formation of lateral clustering patterns observed in living cells. Fluorescence laser-scanning microscopy can be used to image vesicles and cell membranes, and from shape analysis of these images mechanical membrane parameters can be quantified. Methods to analyze images of equatorial sections obtained by confocal or multiphoton microscopy are detailed, in order to estimate curvature, lateral tension, line tension, relative differences in mean curvature and Gaussian curvature bending moduli, and fluorescence dye intensity profiles, typically within coexisting liquid-ordered and liquid-disordered membrane domains. A variety of shape tracing and shape fitting methods are compared.

Key Words: Bending modulus; cholesterol; curvature; domains; energy minimization; fluorescence imaging; force balance; line tension; lipid phases; rafts; sphingomyelin.

1. Introduction

The mechanisms of lateral and spatial membrane organization and their interdependence remain poorly understood (*1*). A number of models (*1–6*) attempt to describe the interactions between proteins and lipids to form functional biological structures (rafts) in cell membranes (*7*), yet consensus is not found on the size, shape, lifetime, and composition of these structures. Despite the tremendous importance and relevance of biological membranes to health and disease (*8–11*), quantitative descriptions of the mechanics and physical chemistry that govern domain formation in model membranes and living cells demand further attention.

Herein, methods to study these phenomena are described. The effects of pressure differences, membrane curvature, bending elasticity, lateral tension, and phase boundary line tension can be measured, compared with theoretical estimates (*12–14*) and related to membrane lipid composition, phase behavior, and lateral organization. In particular, the interest is in fluid-lipid phases that are proposed to exist in living cell membranes: the liquid-ordered (L_o) and liquid-disordered (L_d) phases (*15*). In the L_o phase, acyl chains are relatively densely packed, and thus, conformationally constrained. This results in reduced area per head group, increased bilayer thickness (*12,16*), and increased bending rigidity (*17,18*) but still allows considerable lateral and rotational mobility (*19–21*). On the other hand, in the L_d phase, acyl chains are less constrained, and thus, have higher area per head group, resulting in a thinner bilayer, less orientational order, decreased bending rigidity, and high lateral mobility. The lateral

patterns and out-of-plane morphologies that form in the coexistence of these two phases show a wide range of conformations (17–19,22–25), which reveal mechanics of lipid–lipid (and in more complex systems, lipid–protein and protein–protein) interactions. Thus, studies of such structures and determination of physical shape parameters can be of considerable relevance to the understanding of biological membranes.

2. Biomembrane Models: Giant Unilamellar Vesicles

Giant unilamellar vesicles (GUVs) offer a means to study the forces that control the shapes of membrane bilayers as well as their lateral organization (17,18,22–24,26–29). GUVs do not suffer from the complications introduced by interfacial interactions in solid-supported bilayers and monolayers at the air–water interface, are conveniently prepared (30), and can be easily visualized by light microscopy because of their significantly large size (up to ~100 μm) compared with large and small unilamellar vesicles.

Unilamellar vesicles, in comparison with multilamellar vesicles, are advantageous because the interaction between membrane domains of different phases can be studied. In particular, three-component (ternary) mixtures of a saturated lipid, an unsaturated lipid, and cholesterol (Chol) often exhibit extended regions within the phase diagram of fluid–fluid (L_o – L_d) phase coexistence under a variety of compositions and temperatures. Although this increased number of constituents leads to increased complexity (e.g., compared with two-component mixtures), such three component mixtures are arguably more realistic models of cellular membranes than binary mixtures, and exhibit a surprising number of biologically relevant phenomena and structures even in the absence of protein (17,18,22). **Figure 1** shows an example of a confocal image of a GUV made with a composition (molar ratios) of 1:1:1 sphingomyelin (Spm):*cis*-dioleoylphosphatidylcholine (DOPC):Chol, labeled with fluorescent lipid analogs Bodipy-FL- C_{12} -sphingomyelin and lissamine–rhodamine-B-dioleoylphosphatidylethanolamine (LR-DOPE).

3. Visualization by Laser-Scanning Fluorescence Microscopy

Qualitative characterization of membrane shapes can provide insights into phase behavior and membrane structure, but quantitative analysis is necessary for testing and rejection of some of the contending membrane models. Because of their sensitivity, specificity, and access to a wide range of time-scales ($\sim 10^{-11}$ to $>10^3$ s) with multiple simultaneous labels, fluorescence methods are well suited to studies of membrane structure. Furthermore, confocal and multiphoton microscopy provide an image, which (under well-chosen conditions) is linearly proportional to the concentration of fluorophore within the sample. Therefore, probe partitioning may also be studied using such linear methods wherein ratios of intensities, corrected for difference in probe brightness, correspond to ratios of concentrations to ratios of concentrations.

Fluorescence microscopy methods, of course, depend on the use of fluorescent probes. Key criteria for such probes include: (1) differential partitioning into specific membrane phases, (2) high brightness (photons per fluorophore per second), (3) minimal perturbation of membrane phase behavior, (4) resistance to photobleaching, (5) excitation spectra easily accessible by common lasers, and (6) nonoverlapping emission spectra to minimize channel overlap (bleed-through). Fluorescence microscopy methods are also usually limited by the optical resolution (equal to a fraction of a wavelength, typically approx 250 nm).

Fluorescence microscopy permits acquisition of images over a wide range of time-scales (from $\sim 10^{-3}$ s to days). Multiple fluorophores can be used simultaneously (two to four is

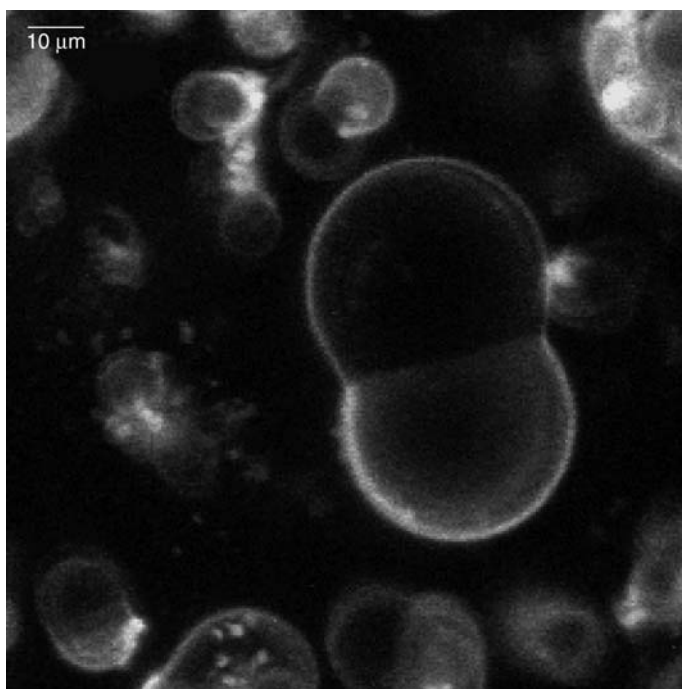


Fig. 1. Confocal z -stack projection of GUVs made with a mixture of egg sphingomyelin, DOPC, and cholesterol, with fluid–fluid (L_o – L_d) phase coexistence at room temperature, labeled with lissamine-rhodamine B-DOPE (LR-DOPE) and Bodipy-FL- C_{12} -sphingomyelin (BFL-Spm). These GUVs were made with a ratio of 1:1:1 Spm: DOPC: Chol by electroformation in 100 mM sucrose and imaged with a Leica TCS-4D confocal microscope using a 60×1.35 NA oil objective, fluorescein emission (515–545 nm) and rhodamine emission (590–660 nm) filters, and excitation with 488 and 568 nm lines from a Krypton-Argon laser.

common), allowing colocalization of lipids and proteins to be quantified. However, fluorescence probes must be carefully chosen. The partitioning of fluorescently labeled lipid analogs often differs significantly from that of the unlabeled original lipid. Spm labeled with a large fluorophore attached to the head group, for example, does not partition in the same way as unlabeled Spm, and changes in the head group strongly affect partitioning. For example, Bodipy-FL- C_{12} -sphingomyelin has been shown to partition into both L_o and L_d phases in GUVs made up of 1:1:1 Chol:DOPC:Egg Spm, whereas Bodipy-TR- C_{12} -sphingomyelin under identical conditions partitions almost exclusively into the L_d phase. Furthermore, probe-partitioning behavior appears to be strongly environment dependent. Perylene, for example, in some regions of the Chol:DOPC:Spm phase diagram partitions preferentially into the L_o phase, but in other regions (e.g., wherein the mole fraction of Spm is lower), does not show a strong preference for either phase. Thus, experiments using perylene can be useful in conjunction with another probe, such as LR-DOPE, which partitions strongly into the L_d phase.

The environment-dependence of probe partitioning is a strong indication that lipids and membrane proteins themselves must have strong environment-dependent partitioning. This dependence is very likely to have significant biological consequences. For example, the introduction of a population of signaling lipid molecules such as phosphatidylinositol 4, 5-*bis*-phosphate into the membrane, could result in change in the local partitioning of proteins with PH

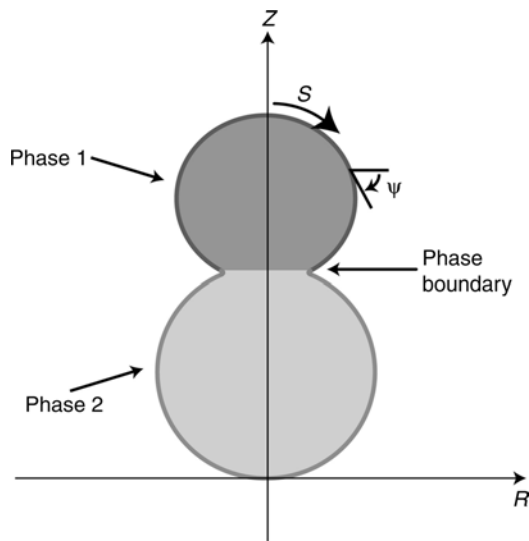


Fig. 2. Equatorial section of an axially symmetric phase-separated GUV. The quantity S is the arc length and ψ is the angle between a tangent to the arc length and the horizontal. Note that the phase boundary and vesicle neck do not necessarily coincide. Differences in Gaussian bending modulus between L_0 and L_d phases, or other conditions, can cause the phase boundary to be shifted toward one phase relative to the neck position (17).

domains near the site of phosphatidylinositol 4, 5-*bis*-phosphate localization. This change in local partitioning could then increase the local concentration to a level wherein the rate of cross-phosphorylation of key proteins becomes significant, leading to a downstream cascade. Evidence for environment-dependent partitioning also suggests that cells could produce and benefit from a variety of local membrane environments regulated to have specific lipid compositions. The following sections discuss experimental methods to obtain membrane traces that can be analyzed in terms of probe-partitioning behavior and membrane geometry.

4. Shape Tracing and Analysis of Equatorial Sections

Equatorial membrane sections may be traced using a variety of algorithms to determine mechanical membrane properties as well as extract information on phase coexistence. For the analysis of a confocal or multiphoton fluorescence image of the equatorial plane of a GUV, two such algorithms (the maximum brightness [MB], and the least squares [LSQ] methods) will be discussed.

Shape analysis of membrane equatorial sections relies fundamentally on determination of the position and angle (orientation) of the membrane obtained by analysis of images, typically from a confocal equatorial slice through the vesicle. From this slice, which is rotated to orient the symmetry (Z) axis in the vertical direction, the R - Z coordinates of the membrane as a function of arc length are determined (see Fig. 2). The angle of the membrane path ψ (measured from the horizontal) and its derivative ψ' as a function of arc length S are then used for numerical analysis of physical shape parameters.

4.1. Tracing in the Direction of Maximum Brightness (MB Method)

The MB algorithm involves following the direction of maximum brightness along the curve of the membrane shape. The algorithm is initiated by manually positioning an marker at some

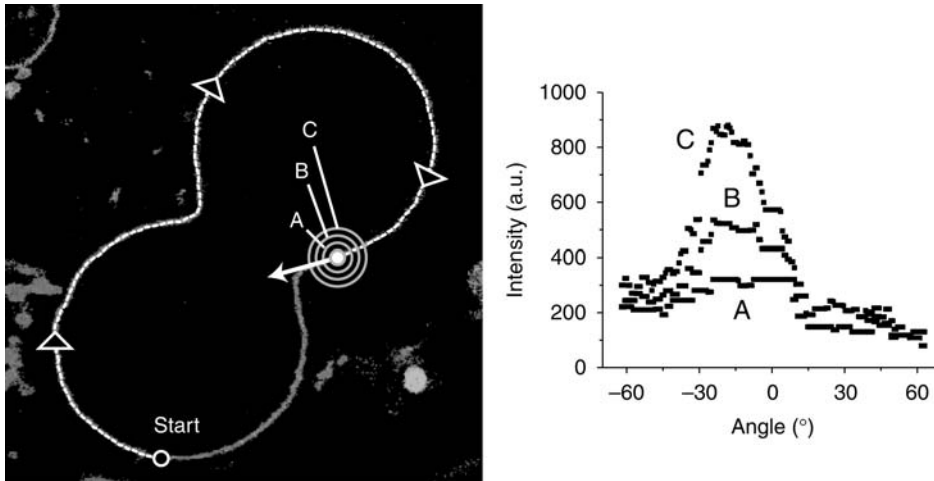


Fig. 3. MB Angular Tracing Algorithm. Shape tracing is accomplished by an automated MATLAB script. A marker (*gray circle with white center*) is initialized manually to a location on the shape (start). Then, the intensity as a function of angle with increasing radius (**curves A,B**) is determined from the pixel values in the image summed up for several radii up to the maximum radius at a given angle (**curve C**). The direction with the maximum intensity (*white arrow*) is then chosen for a small stepwise motion of the marker (and the location and direction recorded). From the new marker location, the process is repeated to trace the entire shape.

point along the membrane shape. Then the intensity profile as a function of angle is determined at several fixed distances from the marker, as shown in **Fig. 3**. The shape is traced by fitting the sum of the intensity profiles at the various radii as a function of angle and determining the direction of maximum intensity turning toward that direction, and then taking a small step. The process is repeated, recording the *x*- and *y*-coordinates, the pixel intensity, the arc length, and the direction angle measured from the *x*-axis. The following section discusses the accuracy of this tracing algorithm.

4.1.1. Estimation of the Uncertainty in Membrane Angles and Curvature Determined by Image Tracing of Equatorial Sections; Determination of Uncertainty by Tracing Ideal Images

Figure 4 shows an example of an ideal image generated from a rasterized circle (representing a membrane 8 pixels wide to avoid pixelization artifacts) blurred by convolution with a Gaussian of width 8 pixels, to which a constant background of pixel value 30 is added. Shot noise is then added to the image assuming a Poisson distribution with the brightest pixel value (i.e., 255) corresponding to $n = \phi \cdot 255$ photons, where ϕ is equal to the number of photons per pixel intensity value. The total number of photons N is then equal to

$$\sum_i n_i = \sum_i \phi p_i$$

where n_i is the number of photons in the *i*-th pixel and p_i is the pixel value in the *i*-th pixel. Note the decrease in noise of $\psi(S)$ and $d\psi/dS$ in **Fig. 5** as the value of ϕ is increased. Thompson

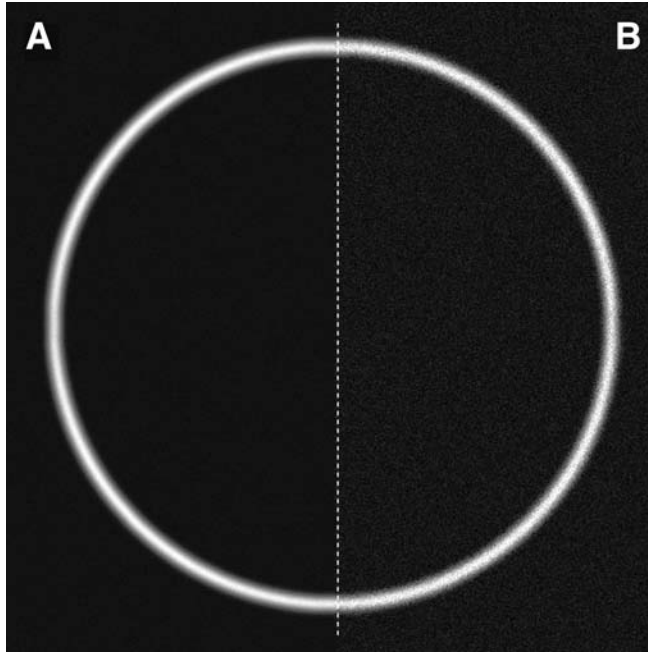


Fig. 4. Theoretical image of a GUV. This image was created using a Matlab program to simulate an image of a spherical GUV with the same visual properties as an image recorded with a confocal microscope. The initial circle has been blurred by convolution with a Gaussian of $1/e^2$ width $R_0 \sim 8$ pixels, had background added, and then shot noise applied. (A) The image has a photon per pixel intensity value of $\phi \sim 4.7$, or approx 25-fold more total photons compared with (B), which has $\phi \sim 0.19$.

et al. (31) calculate the maximum localization precision σ_x for objects smaller than the diffraction-limited resolution, localized in one dimension by fluorescence microscopy:

$$\sigma_x^2 = \frac{r_0^2 + q^2/12}{N} + \frac{4\sqrt{\pi}r_0^3b^2}{qN^2} \quad (1)$$

where r_0 is the standard deviation of the point spread function, N is the number of photons collected, q is the width of the pixel in the image, and b is the background noise. Using σ_x , the error value associated with the angle (σ_ψ) is estimated from the error in the positions of two points ($\sigma_{x_1}, \sigma_{x_2}$) if $\bar{x} = \bar{x}_1 - \bar{x}_2$ and the arc length ΔS between the two points in the limit of small \bar{x} is $|\bar{x}| \approx \Delta S$.

$$\sigma_x^2 = \sigma_{x_1}^2 + \sigma_{x_2}^2 = 2 \left[\frac{r_0^2 + q^2/12}{N} + \frac{4\sqrt{\pi}r_0^3b^2}{qN^2} \right] = 2\rho^2 \quad (2)$$

where ρ is defined as $\rho = \sqrt{\frac{r_0^2 + q^2/12}{N} + \frac{4\sqrt{\pi}r_0^3b^2}{qN^2}}$. From the uncertainty σ_x in the position x , the uncertainty σ_ψ in the angle ψ is estimated (for small angles) as

$$\sigma_\psi = \frac{\sigma_x}{\Delta S} = \frac{\rho}{\Delta S} \sqrt{2} \quad (3)$$

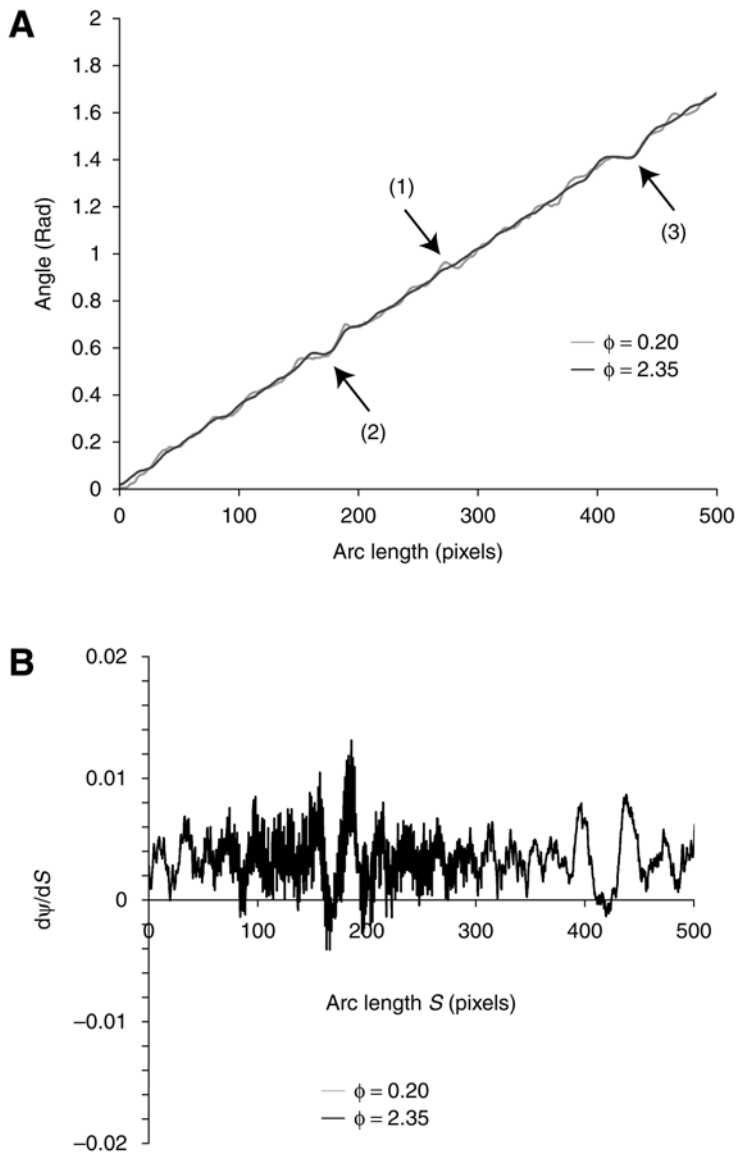


Fig. 5. Effect of image noise on the uncertainty in angles from vesicle traces. **(A)** The resulting angle ψ is shown as a function of arc length S , from a trace of a simulated confocal image of a spherical GUV, for different values of photons per pixel value $\phi = 0.20$ and $\phi = 2.35$. Because the simulated vesicle in this case is circular, the expected result for ψ vs arc length is a straight line. Deviations from this expected behavior are shown by arrows designating **(1)** an example of noise, which decreased when the ϕ increased, as expected for shot noise, and **(2,3)** noise owing to the finite pixel size, which does not decrease with increasing ϕ . **(B)** The resulting curvature ($\psi' = d\psi/dS$) for both traces, corresponding to the same ϕ as in **A**.

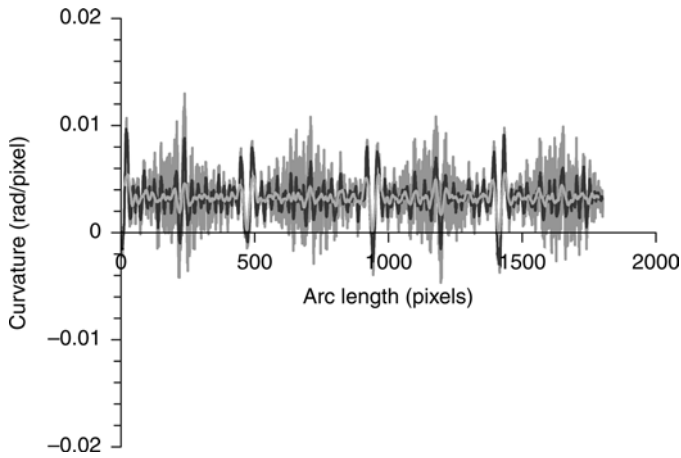


Fig. 6. The effect of smoothing on ψ' as a function of arc length is to reduce noise, in particular noise owing to finite pixel size, which is hard to eliminate for a finite-sized image even with large numbers of line or frame averages. Shown are four complete successive traces of the same circular simulated vesicle whose trace is also shown in Fig. 5. Repeated tracing of the same shape provides a measure of reproducibility (uncertainty) of the tracing algorithm. However, smoothing also reduces the information content of $\psi'(S)$, particularly at high spatial frequencies such as occur at the neck of a sharply pinched shape. Unsmoothed $\psi'(S)$ (medium gray), and smoothed curves with box size 20 (black) and 100 (light gray).

From the values of ψ one can calculate numerically the derivative $d\psi/dS$, or ψ' , which is approximately equal to $\Delta\psi/\Delta S$ for small step size ΔS . Figures 5 and 6 show the ψ and ψ' determined from the trace of a vesicle identical to that shown in Fig. 4 except with $\phi = 0.20$ and $\phi = 2.35$. For a given value of ΔS , this will result in an estimated uncertainty in $\psi' = \frac{d\psi}{dS}$ of

$$\sigma_{\psi'} = \frac{\sigma_{\psi}}{\Delta S} = \frac{\sqrt{2}}{(\Delta S)^2} \sqrt{\frac{r_0^2 + q^2/12}{N} + \frac{4\sqrt{\pi}r_0^3 b^2}{qN^2}} \tag{4}$$

Note that this expression is expected to decrease monotonically as a function of N for all finite N and fixed b . However, in the situation where $\beta = b/N$ is constant (the ratio of background b to total photons N), the expression will approach a limiting value as N becomes large. Such a situation could occur, for example, when the number of emitted signal and background photons is constant but the detection efficiency is changed.

Figure 7 shows the mean squared uncertainty in the curvature $\sigma_{\psi'}$ as determined from traces of a simulated circular vesicle with varying (inverse) numbers of photons. The value of $\sigma_{\psi'}$ does not appear to continue to decrease indefinitely with increasing N , but instead approaches a limiting value of $\sigma_{\psi'} \approx \frac{\beta}{(\Delta S)^2} \sqrt{\frac{8\sqrt{\pi}r_0^3}{q}}$ at large N (i.e., large ϕ), which is consistent with predictions by the model of Thompson et al., but may also include other sources of uncertainties such as from the algorithm itself and differences owing to the one-dimension geometry of the membrane (compared with 2D localization of a spot). Clearly, localization precision will improve as the number of collected signal photons increase, but will only help

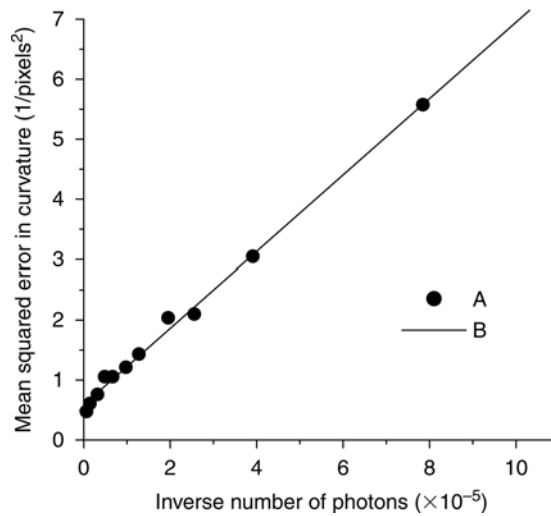


Fig. 7. Effect of number of photons on image tracing accuracy. **(A)** The value of σ_{ψ}^2 equal to the $1/e^2$ width squared of the distribution of curvature values obtained from simulated images, is plotted vs the inverse of N , where N is total number of photons within the region used to estimate that curvature. **(B)** The σ_{ψ}^2 obtained from simulated images was well described by the model of Thompson et al. (see ref. 31) for 2D localization extended here to membrane tracing. The straight line was generated using the actual ratio of background pixel value ($b = 10$) to total photons N ($\beta = b/N = 4.5 \times 10^{-4}$), the pixel size ($a = 1$), the effective arc length per step ($\Delta S = 4$), the total number of photons N , and a value for the resolution ($r_0 = 6.4$ pixels) close to but different from the ideal resolution (8 pixels). For increasing values of N , there is significant improvement in the precision of curvature values determined by the MB algorithm, up to a limiting value (given by the nonzero intercept as $1/N$ goes to zero). For higher values of N (smaller values of $1/N$), σ_{ψ}^2 decreases (and the precision in the curvature increases) less rapidly with N , because of the increased relative contribution of background in these images, which have a constant signal-to-background ratio.

improve the precision in curvature determination (using this algorithm) up to a point that is ultimately limited by signal-to-background ratio. A decrease in the number of microns per pixel (q) will also be necessary to achieve optimal tracing, but this will have the counterproductive effect of spreading the acquired photons out over a larger number of pixels, increasing the fractional uncertainty in the intensity in each pixel. Additionally, smoothing of the measured ψ' can improve the signal-to-noise ratio, whereas adversely affecting the upper limit of resolvable curvature. **Figure 6** shows various boxcar smoothing of the profile of ψ' obtained from **Fig. 4**.

4.2. LSQ Algorithm

Comparison of the MB algorithm and the LSQ algorithm described below, shows that the MB algorithm is particularly sensitive to photon noise and background noise in the image. Thus, acquisition of images that have been averaged over a significant number of frames is necessary to obtain as smooth an image as possible. **Figure 8** explains the LSQ method and shows an example trace for the same simulated spherical vesicle image traced using the MB algorithm discussed previously. The basis of the LSQ algorithm is to use each pixel in the image as a data point, weighted by its uncertainty (estimated as the square root of the number of photons in that pixel), and then fitted by a polynomial (typically of second order) through the data points.

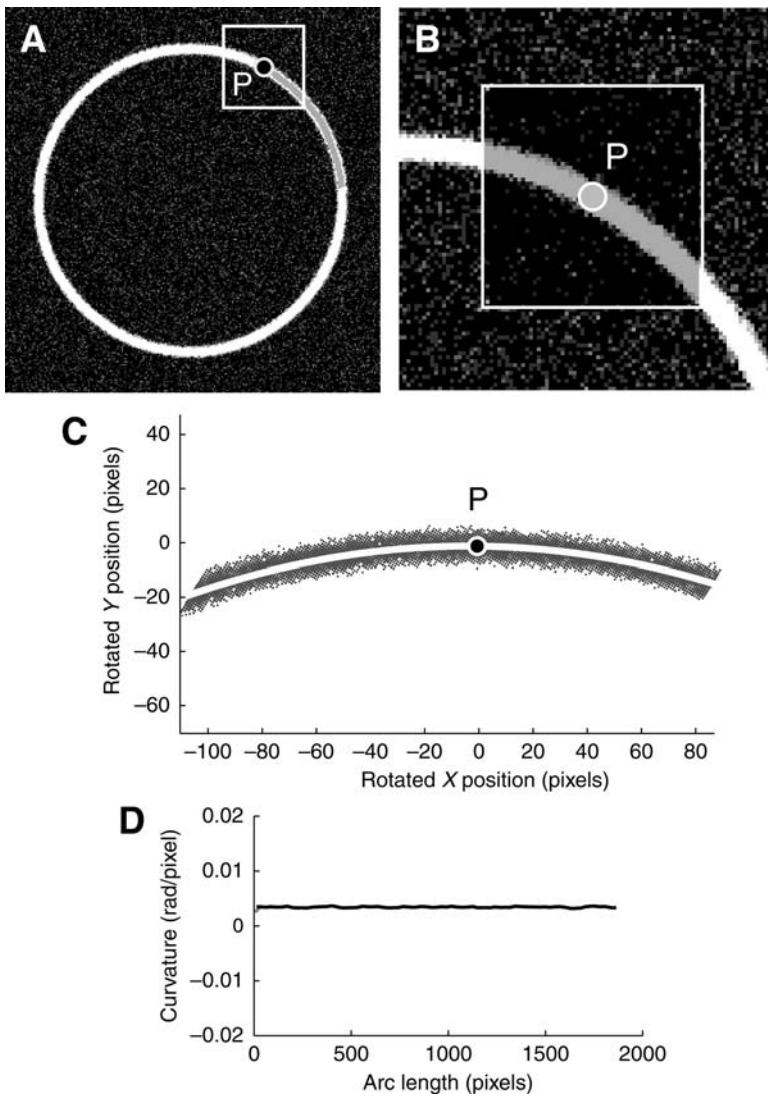


Fig. 8. LSQ vesicle tracing algorithm. The image of an equatorial section of the vesicle is traced by treating the image points as data points, which can be fitted locally with a function $y(x)$. **(A)** Example of a simulated confocal equatorial section of a spherical vesicle with radius 300 pixels, approx 50 photons detected in the brightest pixels, realistic background, and shot noise applied appropriate to the number of photons. The trace (gray line) shown up to the current point (P , black spot with white edge) is calculated by fitting the pixels in the image locally around the point (those within the gray box), each pixel weighted according to the square root of its intensity; **(B)** zoom of image region being fitted. Next, the image within the box is rotated such that the direction along the membrane at P is horizontal (X) and the direction perpendicular to the membrane at P is vertical (Y). The rotated X and Y coordinates for the image shown in the box in **A** and **B** are shown (dark gray points), with LSQ second-order polynomial fit (white line) $y = \alpha x^2 + \beta x + \gamma$ in **C**. Note that the size of each point is equal to the number of photons at the corresponding pixel in the image. The fit is then used to calculate the direction of a step along the membrane, and the value of -2α is equal to the meridional curvature of the membrane at P , shown in **D**. Results from several repeated traces around the vesicle are shown in **D** to demonstrate the reproducibility of the method.

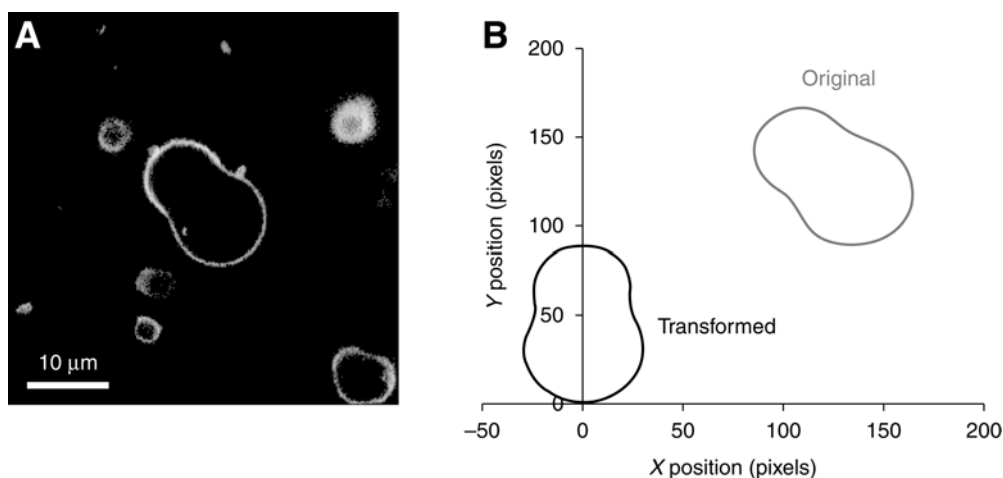


Fig. 9. (A) Example of a GUV made up of egg Spm, DOPC, and cholesterol in the mixture 1:(0.5, 0.5):1 Spm:(*trans*-DOPC: *cis*-DOPC):Chol, created by incubation at 60°C in aqueous 100 mM sucrose, and the fluorescent labels LR-DOPE and bodipy-FL-Spm. This 256 × 256 pixel image is the line-average of 32 successive frames imaged on a Leica TCS-4D confocal microscope using a 60 × 1.35 NA oil objective, fluorescein emission (515–545 nm) and rhodamine emission (590–660 nm) filters, and excitation with 488 and 568 nm lines from a Krypton-Argon laser. The total image size was 50.3 × 50.3 μm² and imaged at 25°C (stage temperature). (B) Rotation and transformation of vesicle trace to center and align the equatorial section of the vesicle with the longitudinal axis of symmetry (in this case the y-axis). Intersection of the trace with the y-axis should be at a 90° angle.

From the fit, the position and curvature of the membrane can be estimated (for further detail, see Fig. 8). Figure 8 also shows that the LSQ algorithm is able to extract the local curvature with improved certainty compared with the MB algorithm: the uncertainties in curvatures in Fig. 8 (LSQ algorithm, unsmoothed) are much smaller for the same image than those shown in Fig. 5 (MB algorithm), even those which were boxcar smoothed shown in Fig. 6 (black and lightgray). Thus, because of the sensitivity of the MB algorithm to typical levels of image noise, particularly on short-length scales, the LSQ algorithm is better suited to portions of the vesicle shape with high curvature, or wherein greater precision in curvature is needed.

4.3. Determination of Area Fractions of L_o and L_d Phases for an Equatorial Section of a Phase-Separated GUV

Area fractions of L_o and L_d phases can be determined directly from an equatorial section of an axially symmetric phase-separated GUV. First, the RGB image (shown in Fig. 9A) is converted to a grayscale image. This grayscale image is traced by the LSQ method using a program written in MATLAB (TheMathworks, Inc. Natick, MA). The starting pixel values for the tracing routine are chosen manually by selecting a coordinate on the vesicle wherein the membrane path is horizontal ($\psi = 0$). Some of the parameters that can be controlled in MATLAB to optimize the trace (Fig. 9B) are the threshold value, the step size, and the maximum turn rate. The output of the shape tracing routine provides x - and y -coordinates, membrane path angles, and pixel intensities (for each channel). The output from the MATLAB

tracing routine is compiled in Microsoft Excel and the transformations below are performed to align the shape to be symmetric with the y -axis:

$$x_1 = \alpha x \cos \theta - \beta y \sin \theta + x_0 \quad (5A)$$

$$y_1 = \alpha x \sin \theta + \beta y \cos \theta + y_0 \quad (5B)$$

where x_1 and y_1 are the transformed x - and y -coordinates, α and β are x and y stretch factors, x_0 and y_0 are x and y offsets, and θ is the rotation angle. The transformation results in a rotated translated shape, shown in **Fig. 9B**. After these transformations, the equatorial section should resemble **Fig. 2**. Each side of the symmetric section is analyzed separately. The equations listed below are used for computing the area fractions. The differential arc length (Δs_i) for the i -th step is determined using $\Delta s_i = \sqrt{(\Delta x_i)^2 + (\Delta y_i)^2}$ where Δx_i and Δy_i are the displacements in x - and y -coordinates, respectively. Thus, the differential area (ΔA_i) for the i -th step in the trace is computed using $\Delta A_i = 2\pi x_i \Delta s_i$, and summed over the entire surface to yield the total area $A_t = \sum \Delta A_i$. Then, the location of the phase boundary is determined by analysis of the intensity as a function of arc length (*see* above), or by manual estimation using image processing software. The area of phase 1 (A_1) is calculated by summing up to the phase boundary and the area of phase 2 (A_2) is obtained from $A_2 = A_t - A_1$, namely, the difference between the total area A_t and the area of the first phase A_1 , where $A_1 = \sum_0^b \Delta A_i$, where b is the location of the phase boundary.

4.4. Analysis of Dye Partitioning in GUVs by Quantification of Fluorescence Intensity

As equatorial sections are traced, the fluorescence intensity can be quantified either at each pixel of the trace or averaged for all pixels within a region centered on the given pixel of the trace. The intensity in both channels is quantified separately and plotted as a function of arc length. **Figure 10** shows the results of an intensity trace of the same GUV image from **Fig. 9**.

The spatial profile of the two dye intensities across the phase boundary can be analyzed for several pieces of information. First, the ratio well inside the phases (after background subtraction) is related to the partition coefficient of the two dyes in the two phases: the LR-DOPE showed 43 ± 27 -fold higher fluorescence in the L_d phase, whereas Bodipy-FL-Spm showed 1.9 ± 0.6 -fold ratio of L_d/L_o fluorescence. Knowing the relative brightness of the probes in these environments, the partition coefficient can be determined. Fluorescence correlation spectroscopy (FCS) is one method, which can in principle be used to determine such concentration and brightness ratios simultaneously. Second, one can extract the position S_{50} , the value of the arc length wherein the dye intensity is halfway between its value well inside the L_o and its value well inside the L_d phase. Differences in S_{50} for different probes may result from an extended phase boundary, differences in dye partitioning behavior, and proximity to a critical point. Third, resolution permitting, in some cases it is possible to determine the profile of the fluorescence intensity across the phase boundary. In many cases the phase boundary will be too sharp to resolve such a profile by light microscopy, because the (spatially narrow) profile will be convolved with a much broader optical point spread function.

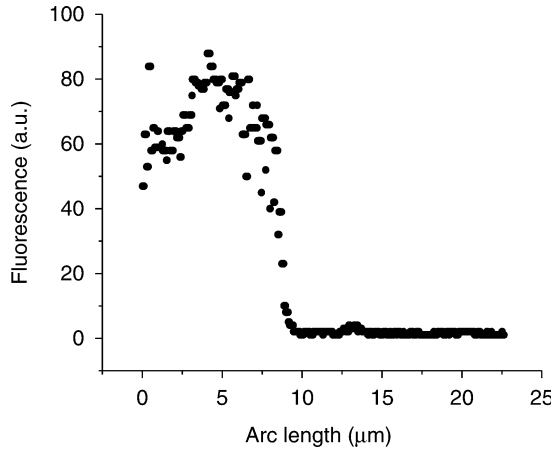


Fig. 10. Plot of fluorescence intensity as a function of arc length S for the **GUV** shown in **Fig. 9**. The red channel (LR-DOPE, a L_d probe) is shown as black circles. The position (as a function of arc length S) at which the fluorescence intensity drops to halfway between the mean in the one phase and the mean in the other phase is defined as S_{50} , in this case $S = 8.43 \pm 0.04 \mu\text{m}$.

5. Shape Analysis of Vesicle Traces

5.1. Shape Fitting Using First Integral of Shape Equations

The analysis is based on determination of the properties that minimize the free energy of the membrane shape. The total free energy of the membrane can be expressed as a sum of contributions (32) from bending energy, inner–outer pressure difference (P), lateral tension (Σ), and phase boundary line tension (σ):

$$F = PV + \sum_{i=1}^n F_b^{(i)} + \Sigma^{(i)} A^{(i)} + \sum_{j=1}^m \sigma^{(j)} \ell^{(j)} \quad (6)$$

summed over each domain i and each phase boundary j , where V is the total vesicle volume, $A^{(i)}$ is the area of the i -th domain, and $\ell^{(j)}$ is the perimeter of the j -th phase boundary. The bending energy terms can be formulated as an integral over the vesicle area:

$$F_b^{(i)} = \frac{\kappa^{(i)}}{2} \int_{A^{(i)}} (C_1 + C_2 - C_0)^2 dA + \kappa_G^{(i)} \int_{A^{(i)}} C_1 C_2 dA \quad (7)$$

and combined with the other terms to yield

$$F = PV + \sum_{i=1}^n \int_{A^{(i)}} \left[\frac{\kappa^{(i)}}{2} (C_1 + C_2 - C_0^{(i)})^2 + \kappa_G^{(i)} C_1 C_2 + \Sigma^{(i)} \right] dA^{(i)} + \sum_{j=1}^m \sigma^{(j)} \ell^{(j)} \quad (8)$$

where C_1 and C_2 are the local radii of curvature of the vesicle around the principal and meridional axes, respectively, $\kappa^{(i)}$ is the mean curvature bending modulus, $\kappa_G^{(i)}$ is the Gaussian curvature bending modulus, and $C_0^{(i)}$ is the spontaneous curvature, for the i -th domain, respectively.

Now shapes with cylindrical (axial) symmetry are considered, which allow to parameterize the vesicle shape in its equatorial plane, along the coordinates of the cylindrical axis Z and

radial axis R , the arc length S along the shape in the equatorial plane, and the angle ψ of the path of the shape as measured from the R axis (see **Fig. 2**). Within this parameterization, Jülicher and Lipowsky (32) show that the total energy can be written for a vesicle with cylindrical symmetry and two-phase domains as

$$F = F_{\text{boundary}} + \int_{A^{(i)}} L dt = \sigma R_{12} + (\kappa_G^{(1)} - \kappa_G^{(2)}) \cos \psi_{12} + \sum_{i=1}^2 2\pi \int_{A^{(i)}} \left[\frac{\kappa^{(i)}}{2} R \frac{dS}{dt} \left(\frac{d\psi}{dt} + \frac{\sin \psi}{R} - C_0^{(i)} \right)^2 + \Sigma^{(i)} R \frac{dS}{dt} + \frac{1}{2} PR^2 \frac{dS}{dt} \sin \psi + \gamma \left(\frac{dR}{dt} - \frac{dS}{dt} \cos \psi \right) \right] dt \quad (9)$$

where the value of F (other than the boundary energy terms F_{boundary}) is calculated by integrating the Lagrangian-like quantity L as a function of t , where t is the independent variable with respect to which R , S , and ψ have been parameterized. At the boundary between phases 1 and 2, R_{12} and ψ_{12} are the radius and angle of the path of the shape, respectively. The parameter γ is a Lagrange multiplier introduced to force the constraint that $\frac{dR}{dt} = \frac{dS}{dt} \cos \psi$, which is a direct consequence of geometry.

The problem can now be solved by variational methods. The free energy has been written as an integral over the shape plus two terms evaluated at the phase boundary, which must be minimized. In classical mechanics, the action or the integral of the Lagrangian (L) over time, is minimized, and typically, a number of relationships between derivatives of L with respect to time and spatial coordinates are obtained. Here, derivatives of F with respect to the coordinates directly follow as a result of $\frac{\partial L}{\partial X} - \frac{d}{dt} \left(\frac{\partial L}{\partial \dot{X}} \right) = 0$, where X is any one of the three coordinates

R , ψ , or S , and \dot{X} denotes the derivative of X with respect to t . These derivatives lead to a set of coupled ordinary differential equations, which can be solved simultaneously to calculate membrane shapes given a known set of shape parameters (i.e., given known values for the bending moduli, the line tension, the pressure difference, and lateral tension). However, in order to extract these same parameters from a vesicle of known shape, one can exploit another important consequence of the minimization of the action-like quantity F . As in classical mechanics the Hamiltonian (kinetic plus potential energy) of a closed system in an inertial frame is a conserved quantity, in this system the analogous quantity

$$H = \sum_{i=1}^2 H^{(i)} = \sum_{i=1}^2 \frac{\kappa^{(i)} R}{2} \left[(\psi')^2 - \left(\frac{\sin \psi}{R} - C_0^{(i)} \right)^2 \right] - \Sigma^{(i)} R - \frac{P}{2} R^2 \sin \psi + \gamma \cos \psi \quad (10)$$

is conserved. In fact, because H is constant at every point along the equatorial vesicle path, it can be evaluated at the poles together with γ to show that $H(t) = H^{(1)} = H^{(2)} = 0$ and that $\gamma = 0$ at both the north and south poles of the shape. Elsewhere, resulting from derivatives of F with respect to γ , Jülicher and Lipowsky find that

$$\gamma' = \frac{\kappa^{(i)}}{2} (\psi' - C_0^{(i)})^2 - \frac{\kappa^{(i)} \sin^2 \psi}{2R^2} + \Sigma^{(i)} + PR \sin \psi \quad (11)$$

Additionally, the following phase boundary jump condition

$$\gamma(S+\varepsilon) = \gamma(S-\varepsilon) + \sigma \quad (12)$$

can be used directly to determine the line tension, given $\gamma(S)$. These results allow to determine the membrane parameters that give the minimum shape energy. Specifically, the set of parameters that results in $H = 0$ (or as near to zero as possible) at all points along the shape are the parameters that yield the lowest shape energy.

Vesicles are imaged by laser-scanning microscopy, and then the image of the equatorial section of the vesicle is traced to find R , ψ , and S . Because H contains only the quantity γ that must be obtained by integration of γ' , and because γ' depends only on the shape and the shape parameters, one can iteratively guess a set of parameters, calculate γ' , and integrate with respect to S to get γ . Then, determine H , and test whether that set of parameters gives the smallest possible value (value closest to zero) for H everywhere along the path. The parameters are thus adjusted, so that the sum of $[H(S)]^2$ summed over each point in the vesicle is minimized. The parameters, which can in principle be considered are $\kappa^{(i)}$, $\kappa_G^{(i)}$, $\Sigma^{(i)}$, P , $C_0^{(i)}$, and σ , but the overall energy is arbitrary within a multiplicative constant equal to one of the bending moduli. Therefore, shapes are fitted with the value of $\kappa^{(1)}$ fixed to unity, and values of fitting parameters relative to one bending modulus are quoted (typically the bending modulus of the L_d phase, which has been estimated experimentally for a few pure lipidic systems).

As primarily bilayers made up of phospholipids and Chol are being considered, and the rate of Chol flip-flop is high, effects because of differences in number densities of lipids in the opposing monolayer leaflets can be neglected (32,33); spontaneous curvatures are also typically neglected, although in principle may be included. This procedure is accomplished using a computer program written in MATLAB. Column vectors containing S , R , ψ , and $d\psi/dS$ are determined from shape tracing algorithms (*see* above), and used as inputs to the program along with initial guesses at the shape parameters and the location of the phase boundary. The routine then searches using the `fminsearch` function for the minimum sum of $[H(S)]^2$ evaluated at all points along the equatorial section. This method has the advantage that it starts with the experimentally observed shape, which by definition incorporates the constraints on the total area, area fraction, and total volume for the shape.

5.2. Shape Fitting Through Full Integration of Differential Shape Equations

It was shown in the previous section that line tension estimates, lateral tension, normal pressure difference, and the relative bending stiffness in vesicles with fluid phase coexistence can be obtained from adjusting fit parameters in a conserved zero value Hamiltonian-like function of the experimentally obtained vesicle geometry, in terms of radius R , tangent angle ψ , and derivative of tangent angle with respect to arclength ψ' . An advantage of this approach is that a complete integration of differential shape equations to yield a fitted vesicle shape is not necessary, which minimizes computational efforts. A disadvantage of the Hamiltonian fit method is the high uncertainty of fit parameters that appear only in the jump conditions of the shape equations at the phase boundary (but not in the bulk differential shape equations). These parameters include the relative mean curvature bending stiffness, as well as the relative Gauss curvature stiffness difference.

The comparison of fully integrated theoretical vesicle shapes with experimentally obtained vesicle shapes can yield estimates for both mean curvature and Gauss curvature differences

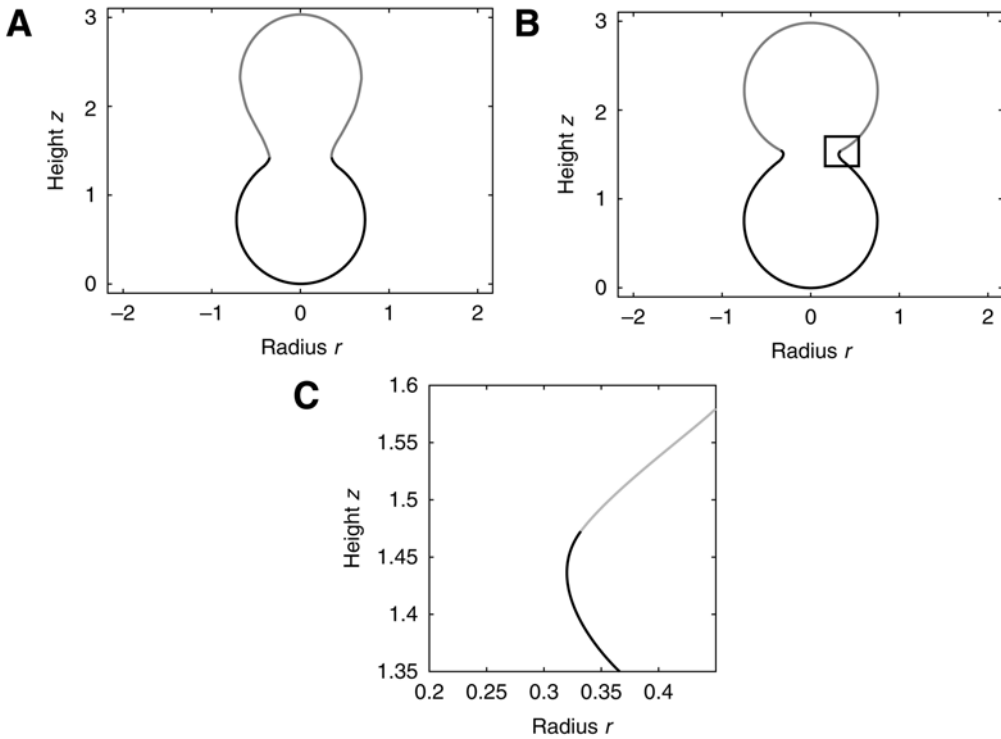


Fig. 11. Vesicles with fixed line tension, deformed by differing mechanical effects. All vesicles have the same volume of 76% of the volume of a sphere. Furthermore, all vesicles have the area of a sphere with unit radius. (A) The mean curvature stiffness of the gray phase is a factor of 100 higher compared with the black phase, but there is no difference in Gaussian bending stiffness. (B) The Gaussian bending stiffness of the black phase is higher [$\hat{\Delta}_g = (\kappa_g^{\text{black}} - \kappa_g^{\text{gray}}) / \kappa^{\text{black}} = 3$] than the gray phase, but the two phases have equal mean curvature stiffness. (C) Inset of the right phase boundary (vesicle neck) of the vesicle shown in B.

between fluid-ordered and -disordered phases (17). This finding follows from the observation that differing mean and Gauss curvature moduli have characteristically differing effects on experimental vesicle shapes. **Figure 11A** shows a vesicle with equal area fraction and Gaussian bending stiffness, but a much higher mean curvature modulus in the gray membrane phase versus the black phase. The membrane phase with the higher bending stiffness forms a droplet or pear shape, whereas the phase with smaller bending stiffness shows the shape of a truncated sphere. In contrast to differing mean curvature moduli, a difference in Gaussian bending stiffness leads to a vesicle deformation that is localized to the phase boundary.

Figure 11 indicates that the phase with the smaller resistance toward Gauss curvature forms the high curvature neck, i.e., the phase boundary is shifted out of the neck. This phenomenon was theoretically described by Jülicher et al. (34). Furthermore, increasing line tension leads to increase of curvature at the phase boundary of a phase separated vesicle, as indicated in **Fig. 12**, wherein a vesicle with fixed reduced volume of 0.76 is successively deformed by increasing line tension. Deformation leads to a limit shape that is described by truncated spheres with constant curvature, connected at the phase boundary.

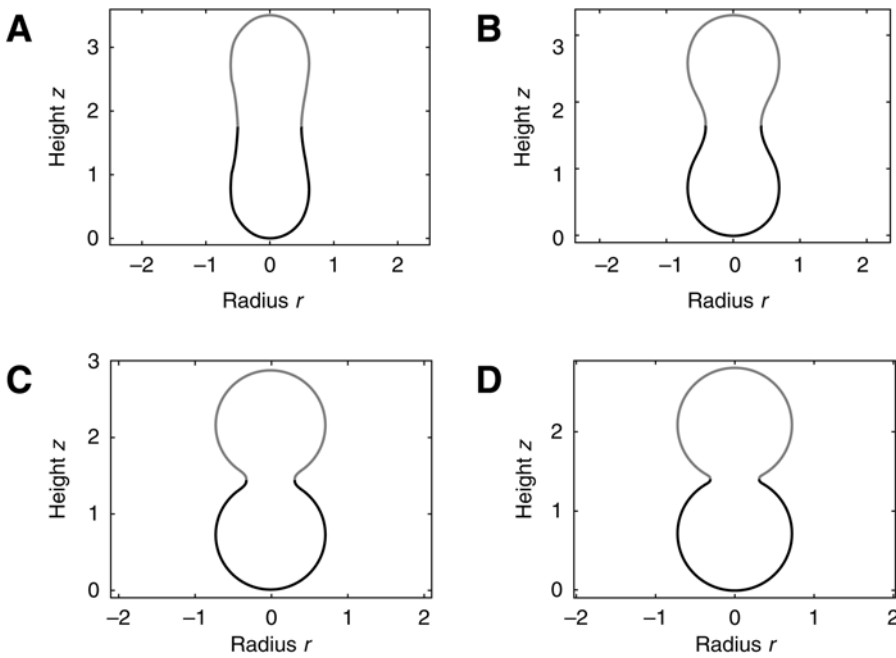


Fig. 12. Vesicles with the same bending stiffness (equal mean and Gauss curvature moduli), equal volume, and an area equal to a unit sphere, but increasing line tension. From **A–D** the line tension increases with values of 0, 2, 50, and 500, respectively. In all cases, the vesicle volume had a constant value of 76% from the volume of a sphere with the area of a unit sphere.

The following section describes, from a mechanical point of view, the terminology and shape equations that allow comparison between experimental and theoretical vesicle shapes. The shape equations obtained from balancing forces and moments in membrane area elements are equivalent to the shape equations described previously, which are derived from minimizing the global mechanical energy. The out-of-plane bulk force balance equation can be expressed as (35–37)

$$Q' + \frac{\cos \psi}{R} Q - T_m \psi' - \frac{\sin \psi}{R} T_p - p = 0 \tag{13}$$

where Q is the transverse (i.e., along the surface normal) shear per unit length acting on an edge along the parallels, a prime indicates a derivative with respect to arclength, T_m and T_p are lateral stress components along the meridian and parallels, respectively, and p is a pressure difference across the membrane acting along the *inward* surface normal direction (i.e., p is an *outer excess* pressure). The in-plane balance of forces can be written as

$$T_m + \frac{\cos \psi}{R} (T_m - T_p) + Q \psi' = 0 \tag{14}$$

The jump conditions originally derived by Jülicher and Lipowsky (32) can be expressed as (17)

$$T_{mL_d} - T_{mL_o} - \sigma \frac{\cos \psi}{R} = 0, \tag{15}$$

for the jump in lateral stress, where L_d indicates the value before and L_o the value after the phase jump (in the direction away from the north pole of the vesicle), respectively, in a vesicle with L_o phase oriented toward the north pole. The jump condition for transverse shear is

$$Q_{L_d} - Q_{L_o} - \sigma \frac{\sin \Psi}{R} = 0 \tag{16}$$

Accordingly, the jump in lateral stress is equal to line tension multiplied by the geodesic curvature ($\cos \psi/R$) along the boundary, whereas the jump in transverse shear is the line tension multiplied by the principal curvature along the boundary. It can be shown that tensions T_m and T_p and transverse shear Q are related to curvature, mean curvature bending resistance, κ , and mean tension, d , in the membrane (38) by $T_m = -[d - 2 \kappa h (\psi' + h)]$, $T_p = -[d + 2 \kappa h (\psi' + h)]$, and $Q = -2\kappa h'$. The Gaussian curvature resistance modulus κ_G enters the condition for zero jump in moments across the boundary, $M_{mL_d} - M_{mL_o} = 0$, through the constitutive equation $M_m = -(2 \kappa h - \kappa_G \sin \psi / R)$ (32,38).

To solve the system of differential shape equations for a membrane with coexisting phases, all mechanical parameters are expressed relative to a given bending stiffness of one of the two coexisting phases (see above) (32): $\epsilon = \kappa^{L_o} / \kappa^{L_d}$ is the ratio between the mean curvature bending rigidities of the two regions, $\hat{\Delta}_g = (\kappa_g^{L_d} - \kappa_g^{L_o}) / \kappa^{L_d}$ provides a measure of the difference in Gaussian curvature rigidities between the two regions, and dimensionless transverse shear, line tension, mean lateral tension, and pressure, respectively are

$$\hat{Q} = \frac{QR_0^2}{\kappa^{L_d}}, \quad \hat{\sigma} = \frac{\sigma R_0}{\kappa^{L_d}}, \quad \hat{d} = \frac{dR_0^2}{\kappa^{L_d}}, \quad \text{and} \quad \hat{p} = \frac{pR_0^3}{\kappa^{L_d}}, \tag{17}$$

where R_0 is the radius of a spherical membrane (vesicle) with the same area as the particular deformed vesicle. All further quantities bearing the dimension of length are nondimensionalized by R_0 as well. The shape equations are simultaneously solved in the L_o and L_d regions of the membrane subject to appropriate boundary conditions.

The six quantities \hat{Q} , h , ψ , R , z , and \hat{d} , are chosen as dependent variables, where z is the vesicle height (see Fig. 11), whereas the arclength s is the independent variable. For each phase of a membrane with domains, a set of six coupled first order differential equations is obtained. Two of these are derived from Eqs. 14 and 15, and read for the L_o region (i.e., the region before the phase jump, viewed from the north pole of the vesicle)

$$\hat{Q}' = \frac{\cos \Psi}{R} \hat{Q} + 2h \left[\hat{d} + \epsilon h^2 + \epsilon \frac{\sin \Psi}{R} \left(2h + \frac{\sin \Psi}{R} \right) \right] + \hat{p} \tag{18}$$

and

$$h' = -\hat{Q} / \epsilon. \tag{19}$$

The four remaining equations are $\psi' = -2h - \sin \psi / R$,

$$R' = \cos \psi, \quad z' = \sin \psi, \quad \text{and} \quad \hat{d}' = 0.$$

The six equations for the L_d region are identical, except that the parameter ϵ in Eqs. 18 and 19 does not appear (because of scaling with respect to κ^{L_d}). The 12 boundary conditions at

north pole ($s = 0$), phase discontinuity ($s = s^*$), and south pole ($s = s_c$) are $Q_s(0) = Q_s(s_c) = 0$, $\psi(0) = 0$, $\psi(s_c) = \pi$, $r(0) = 0$, $z(0) = 0$, the continuity equations $\psi(s^{*L_o}) = \psi(s^{*L_d})$, $R(s^{*L_o}) = R(s^{*L_d})$, $z(s^{*L_o}) = z(s^{*L_d})$, and finally, the three jump conditions obtained from Eqs. 15 and 16, and $M_{mL_d} - M_{mL_o} = 0$:

$$\hat{Q}_{L_d} - \hat{Q}_{L_o} - \hat{\sigma} \frac{\sin \Psi}{R} = 0, \quad (20)$$

$$\hat{d}^{L_d} - \hat{d}^{L_o} + h^{L_d 2} - \varepsilon h^{L_o 2} + (h^{L_d} - \varepsilon h^{L_o}) \frac{\sin \Psi}{R} + \hat{\sigma} \frac{\cos \Psi}{R} = 0, \quad (21)$$

and

$$h^{L_d} - \varepsilon h^{L_o} - \hat{\Delta}_g \frac{\sin \Psi}{R} = 0. \quad (22)$$

It can be shown that $R(s_c) = 0$ is automatically satisfied. The choice of a continuous tangent angle over the phase boundary is based on experimental evidence in vesicles with fluid phase coexistence (see ref. 18). To account for the constraints on total membrane area and area fraction of the coexisting phases of a phase-separated lipid vesicle at constant temperature, the generalized variable t is introduced (32), such that $s(t = 0) = 0$, $s(t^*) = s^*$, $s(t_c) = s_c$, and $\dot{s} \equiv ds/dt$. Derivatives with respect to s are thus expressed in terms of derivatives with respect to t , for example, $Q'_s \dot{s} = \dot{Q}$. The differential shape equations of the (L_o) and (L_d) regions are solved by mapping t^{L_o} in the range $[0, t^*]$ and t^{L_d} in the range $[t^*, \pi]$ onto the common interval $[0, \pi]$.

The arclength of the deformed vesicle is obtained by simultaneously integrating $\dot{s} = \sin(t)/R$, with the boundary condition $s(t = 0) = 0$. The singularities at the poles are approximated by expansions near the poles. The pressure difference, \hat{p} , is either prescribed or, in case of a fixed volume V_p , can be obtained as an eigenvalue of the boundary value problem, with introduction of the additional differential equation $\dot{V} = \pi r \sin \psi \sin t$, with boundary conditions $V(t = 0) = 0$ and $V(t = \pi) = V_f$. Two additional boundary values can be determined from the experimental shape. These are the radius R and tangent angle ψ at the phase boundary.

Defining these experimentally measured geometric parameters as boundary values in the numerical boundary value problem solver, allows determination of additional mechanical parameters as eigenvalues. These are the line tension at the phase boundary, and normalized difference between Gaussian curvature moduli $\hat{\Delta}_g = (\kappa_g^{L_d} - \kappa_g^{L_o}) / \kappa^{L_d}$.

Vesicle geometries can thus be numerically generated, which have a vesicle volume, boundary radius, and tangent angle equal to the experimental shape. Varying the single fit parameter ε , the ratio between mean curvature bending modulus of L_o and L_d phase, respectively, allows to obtain a best fit to the experimental vesicle shape by LSQ fitting of numerical shapes to experimentally determined shapes.

6. Conclusion

In summary, the experimental acquisition and subsequent quantitative analysis of vesicle shape traces in terms of two shape-tracing algorithms have been described. Besides the vesicle trace, the intensity profile along the vesicle trace can be determined. Furthermore, numerical

methods were developed to examine the mechanics of vesicle shapes. A Hamiltonian fit method was devised, which allows quantification of line tension, lateral tensions, pressure difference, and ratio of mean curvature bending moduli (**18**). Full integration of the shape equations allows the determination of Gaussian bending stiffness differences between coexisting fluid phases. The experimental and numerical methods of vesicle shape analysis herein described are likely to provide additional insight into the mechanics and physical chemistry of membrane systems more complex than those described in this chapter. For example, an important and biologically relevant extension of the approach described herein is to consider membranes with intrinsic curvature preference (spontaneous curvature) that is caused, for example, by the binding of peripheral membrane proteins.

Acknowledgments

The authors thank Dr. Joshua Zimmerberg and Dr. Paul Blank for the use of the confocal microscope. The work described was supported in part by grant no. 1-K25-AI-65459-01 from the National Institute of Allergy and Infectious Diseases. Its contents are solely the responsibility of the authors and do not necessarily represent the official views of the National Institute of Health.

References

1. Anderson, R. G. W. and Jacobson, K. (2002) Cell biology—A role for lipid shells in targeting proteins to caveolae, rafts, and other lipid domains. *Science* **296**, 1821.
2. Sharma, P., Varma, R., Sarasij, R. C., et al. (2004) Nanoscale organization of multiple GPI-anchored proteins in living cell membranes. *Cell* **116**, 577.
3. Fujiwara, T., Ritchie, K., Murakoshi, H., Jacobson, K., and Kusumi, A. (2002) Phospholipids undergo hop diffusion in compartmentalized cell membrane. *J. Cell Biol.* **157**, 1071.
4. Nakada, C., Ritchie, K., Oba, Y., et al. (2003) Accumulation of anchored proteins forms membrane diffusion barriers during neuronal polarization. *Nat. Cell Biol.* **5**, 626.
5. Edidin, M. (2003) Lipids on the frontier: a century of cell-membrane bilayers. *Nat. Rev. Mol. Cell Biol.* **4**, 414.
6. Kwik, J., Boyle, S., Fooksman, D., Margolis, L., Sheetz, M. P., and Edidin, M. (2003) Membrane cholesterol, lateral mobility, and the phosphatidylinositol 4,5-bisphosphate-dependent organization of cell actin. *Proc. Natl. Acad. Sci. USA* **100**, 13,964.
7. Simons, K. and Ikonen, E. (1997) Functional rafts in cell membranes. *Nature* **387**, 569.
8. Manes, S., del Real, G., and Martinez, C. (2003) Pathogens: Raft Hijackers. *Nat. Rev. Immun.* **3**, 557.
9. Marks, D. L. and Pagano, R. E. (2002) Endocytosis and sorting of glycosphingolipids in sphingolipid storage disease. *Trends Cell Biol.* **12**, 605.
10. Pagano, R. E., Puri, V., Dominguez, M., and Marks, D. L. (2000) Membrane traffic in sphingolipid storage diseases. *Traffic* **1**, 807.
11. Takeda, M., Leser, G. P., Russell, C. J., and Lamb, R. A. (2003) Influenza virus hemagglutinin concentrates in lipid raft microdomains for efficient viral fusion. *Proc. Natl. Acad. Sci. USA* **100**, 14,610.
12. Kuzmin, P. I., Akimov, S. A., Chizmadzhev, Y. A., Zimmerberg, J., and Cohen, F. S. (2005) Line tension and interaction energies of membrane rafts calculated from lipid splay and tilt. *Biophys. J.* **88**, 1120.
13. Lipowsky, R. (1992) Budding of Membranes Induced by Intramembrane Domains. *J. Physique II* **2**, 1825.
14. Shi, Q. and Voth, G. A. (2005) Multi-scale modeling of phase separation in mixed lipid bilayers. *Biophys. J.* **89**, 2385.
15. Brown, D. A. and London, E. (2000) Structure and function of sphingolipid- and cholesterol-rich membrane rafts. *J. Biol. Chem.* **275**, 17,221.

16. Akimov, S. A., Kuzmin, P. I., Zimmerberg, J., Cohen, F. S., and Chizmadzhev, Y. A. (2004) An elastic theory for line tension at a boundary separating two lipid monolayer regions of different thickness. *J. Electroanal. Chem.* **564**, 13.
17. Baumgart, T., Das, S., Webb, W. W., and Jenkins, J. T. (2005) Membrane elasticity in giant vesicles with fluid phase coexistence, *Biophys. J.* **89**, 1067.
18. Baumgart, T., Hess, S. T., and Webb, W. W. (2003) Imaging coexisting fluid domains in biomembrane models coupling curvature and line tension. *Nature* **425**, 821.
19. Veatch, S. L. and Keller, S. L. (2005) Seeing spots: Complex phase behavior in simple membranes. *Biochim. Biophys. Acta*
20. Ipsen, J. H., Karlstrom, G., Mouritsen, O. G., Wennerstrom, H., and Zuckermann, M. J. (1987) Phase-Equilibria in the Phosphatidylcholine-Cholesterol System. *Biochim. Biophys. Acta* **905**, 162.
21. Filippov, A., Oradd, G., and Lindblom, G. (2003) The effect of cholesterol on the lateral diffusion of phospholipids in oriented bilayers. *Biophys. J.* **84**, 3079.
22. Veatch, S. L. and Keller, S. L. (2003) A closer look at the canonical raft mixture in model membrane studies. *Biophys. J.* **84**, 725.
23. Veatch, S. L. and Keller, S. L. (2002) Organization in lipid membranes containing cholesterol. *Phys. Rev. Lett.* **89**, art. no.
24. Feigenson, G. W. and Buboltz, J. T. (2001) Ternary phase diagram of dipalmitoyl-PC/dilauroyl-PC/cholesterol: Nanoscopic domain formation driven by cholesterol. *Biophys. J.* **80**, 2775.
25. Bacia, K., Schwille, P., and Kurzchalia, T. (2005) Sterol structure determines the separation of phases and the curvature of the liquid-ordered phase in model membranes. *Proc. Natl. Acad. Sci. USA* **102**, 3272.
26. Bagatolli, L. A. (2003) Thermotropic behavior of lipid mixtures studied at the level of single vesicles: giant unilamellar vesicles and two-photon excitation fluorescence microscopy. *Methods Enzymol.* **367**, 233.
27. Bagatolli, L. A. and Gratton, E. (2000) Two photon fluorescence microscopy of coexisting lipid domains in giant unilamellar vesicles of binary phospholipid mixtures. *Biophys. J.* **78**, 290.
28. Korlach, J., Baumgart, T., Webb, W. W., and Feigenson, G. W. (2005) Detection of motional heterogeneities in lipid bilayer membranes by dual probe fluorescence correlation spectroscopy. *Biochim. Biophys. Acta* **1668**, 158.
29. Korlach, J., Schwille, P., Webb, W. W., and Feigenson, G. W. (1999) Characterization of lipid bilayer phases by confocal microscopy and fluorescence correlation spectroscopy. *Proc. Natl. Acad. Sci. USA* **96**, 8461.
30. Mathivet, L., Cribier, S., and Devaux, P. F. (1996) Shape change and physical properties of giant phospholipid vesicles prepared in the presence of an AC electric field. *Biophys. J.* **70**, 1112.
31. Thompson, R. E., Larson, D. R., and Webb, W. W. (2002) Precise nanometer localization analysis for individual fluorescent probes. *Biophys. J.* **82**, 2775.
32. Julicher, F. and Lipowsky, R. (1996) Shape transformations of vesicles with intramembrane domains. *Phys. Rev. E* **53**, 2670.
33. Seifert, U., Berndl, K., and Lipowsky, R. (1991) Shape Transformations of Vesicles—Phase-Diagram for Spontaneous-Curvature and Bilayer-Coupling Models. *Phys. Rev. A* **44**, 1182.
34. Julicher, F. and Lipowsky, R. (1993) Domain-Induced Budding of Vesicles. *Phys. Rev. Lett.* **70**, 2964.
35. Evans, E. and Yeung, A. (1994) Hidden Dynamics in Rapid Changes of Bilayer Shape. *Chem. Phys. Lipids* **73**, 39.
36. Evans, E. A. and Skalak, R. (1980) *Mechanics and Thermodynamics of Biomembranes*. CRC Press, Boca Raton, FL.
37. Powers, T. R., Huber, G., and Goldstein, R. E. (2002) Fluid-membrane tethers: Minimal surfaces and elastic boundary layers. *Phys. Rev. E* **65**.
38. Jenkins, J. T. (1976) Static equilibrium configurations of a model red blood cell. *J. Math. Biol.* **4**, 149.